Nuclear Instruments and Methods in Physics Research A 817 (2016) 46–56

Contents lists available at ScienceDirect

Nuclear Instruments and Methods in Physics Research A

journal homepage: www.elsevier.com/locate/nima

Beam studies at the SPEAR3 synchrotron using a digital optical mask

H.D. Zhang [a,b,c,*], R.B. Fiorito [a,b,c], J. Corbett [d], A.G. Shkvarunets [a], K. Tian [d], A. Fisher [d]

[a] Institute for Research in Electronics and Applied Physics, University of Maryland, College Park, MD 20742, United States
[b] Cockcroft Institute, Daresbury Sci Tech, Warrington WA4 4AD, United Kingdom
[c] Department of Physics, University of Liverpool, Liverpool L69 7ZE, United Kingdom
[d] SLAC, Menlo Park, CA 94650, United States

ARTICLE INFO

Article history:
Received 12 January 2016
Accepted 23 January 2016
Available online 29 January 2016

Keywords:
Synchrotron diagnostics
Injection
Digital micro-mirror-array device
Optical mask
Optical synchrotron radiation beam line
Stanford positron electron asymmetric ring

ABSTRACT

The 3GeV SPEAR3 synchrotron light source operates in top-up injection mode with up to 500 mA circulating in the storage ring (equivalently 392 nC). Each injection pulse contains 40–80 pC producing a contrast ratio between total stored charge and injected charge of about 6500:1. In order to study transient injected beam dynamics during user operations, it is desirable to optically image the injected pulse in the presence of the bright stored beam. In the present work this is done by imaging the visible component of the synchrotron radiation onto a digital micro-mirror-array device (DMD), which is then used as an optical mask to block out light from the bright central core of the stored beam. The physical masking, together with an asynchronously-gated, ICCD imaging camera, makes it possible to observe the weak injected beam component on a turn-by-turn basis. The DMD optical masking system works similar to a classical solar coronagraph but has some distinct practical advantages: i.e. rapid adaption to changes in the shape of the stored beam, a high extinction ratio for unwanted light and minimum scattering from the primary beam into the secondary optics. In this paper we describe the DMD masking method, features of the high dynamic range point spread function for the SPEAR3 optical beam line and measurements of the injected beam in the presence of the stored beam.

1. Introduction

Beam 'halo' measurements using optical synchrotron radiation have been previously carried out at the KEK-PF synchrotron using a fixed-mask coronagraph technique [1,2]. Recently, we have modified this method; we employ a programmable digital micro-mirror-array device (DMD) to provide an optical mask based on either a prescribed geometric shape or an intensity threshold level. This technique has been used to image the halo of electron beams at the University of Maryland Electron Ring (UMER) and the Jefferson Laboratory's Electron Recovery Linac [3,4]. Similar to a coronagraph, the mask created with the DMD blocks out the emission from the bright background source (i.e. the beam 'core') and re-images the light surrounding the core. However, in contrast to the coronagraph which uses a fixed-mask size, the DMD can be quickly reconfigured to conform to changes in the shape of the beam core. In addition, the DMD deflects light from the beam core 48° away from the optical axis with a high extinction ratio ($>1000:1$), before it can reach the secondary optics downstream of the DMD. This greatly reduces the forward scattering of light from the high intensity beam core into the secondary optics used to image the beam halo.

The resolution and dynamic range of any optical system is characterized by the point spread function (PSF) which is the spatial intensity distribution in the image plane of a point source in the object plane. The PSF is affected by diffraction and other effects such as aberrations and scattering in the optics. Since diffraction is usually the primary effect in determining the image resolution and the dynamic range, the PSF is commonly calculated from diffraction theory. It is the low-intensity wings of the PSF that limit the measurement of the beam halo, or in the case of the present study, the weak injected beam. Therefore, in order to be assured that one is actually measuring the halo (or faithfully observing the injected beam), the PSF should be determined, preferably experimentally, using a small 'point' source that has the same angular distribution of the radiation being imaged. For this purpose the stored beam is a convenient point like source, since it is much smaller than the injected beam before it gets damped and very stable when measured alone, i.e. when there is no injection of charge into the ring. The PSF can also be theoretically calculated. In this paper we do this by using a simulated aperture function (i.e. the light distribution at the face of the first objective lens of the

* Corresponding author at: Cockcroft Institute, Daresbury Sci Tech, Warrington WA4 4AD, United Kingdom.
E-mail address: hao.zhang@cockcroft.ac.uk (H.D. Zhang).

http://dx.doi.org/10.1016/j.nima.2016.01.071
0168-9002/

system) that has the same characteristics of the light observed experimentally.

In the experiments performed on SPEAR3 we used the DMD masking technique to make high dynamic range composite images of the stored beam which is known from calculation and other measurements to be $\sim$140 μm (H) × 20 μm (V) [5,6]. Though this source is not actually a point, it is sufficiently small and far from the imaging optics to reveal the dominant features of the PSF with a high dynamic range (10^{-4}). In this paper we demonstrate that the main features of the PSF of the optical beam line at SPEAR3 are due to diffraction from rectangular-shaped apertures in the optical path located upstream of the first objective lens of the visible optics train. Diffraction from these rectangular apertures dominates over any other diffraction introduced by the lenses or other optical elements downstream of the objective lens. We confirm these results with our own numerical simulation code designed to calculate the PSF of the optical diagnostics beam line.

We further demonstrate that by applying a DMD mask at the image plane of the first objective and masking the image of the stored beam it is possible to view the weak injected beam in the presence of the bright stored beam during the so-called 'User' mode. With this technique it is possible to study the turn-by-turn evolution of its transverse profile during charge accumulation. In this case the injected beam plays the role of the low-intensity beam halo observed in previous studies at UMER and JLAB. The SPEAR3 studies are important not only to confirm proper accelerator operation but also to understand charge capture dynamics. The measurements provide insight into the physics of beam capture which is important for injection efficiency, insertion device protection and radiation physics. The measurements are also important to validate matching between the transport line and storage ring beta-functions.

Regarding to the beam diagnostic using visible synchrontron radiation, there are many reference [7–11] based on several site-specific examples. However, the experiment study of the injected beam is few. Previous studies of the injected beam at SPEAR3 were limited to conditions with no charge accumulation in order to protect the Intensified CCD camera (Roper PiMax, Princeton Instruments) from saturation by the high intensity stored beam [12]. For injected beam studies, if the charge were permitted to damp down and accumulate, the visible synchrotron radiation (SR) 'core' beam would quickly saturate or possibly damage the image sensor. Thus some type of optical masking is required in order to observe the injected beam during the charge accumulation. To our knowledge this has not be done previously. As illustrated in Fig. 1, the evolution of the injected beam charge distribution can be complex as the circulating pulse passes through the non-linear lattice magnets leading to charge filamentation and decoherence within the 6-D phase space volume. It is important to note that the transverse projection of the charge distribution integrates and thus smooths over otherwise complicated beam structure in the longitudinal direction [12,13].

Quantitatively the ratio of charge stored in a typical single SPEAR3 bunch to charge contained in a single injected pulse is about 20:1. Furthermore the ratio of transverse injected beam size for the first few turns to stored beam size is about 10:1, so the net contrast ratio is of order 10^2. In practice however the stored beam contains up to 300 bunches so the intensity contrast between SR emitted from the stored beam to SR emitted from a single injector pulse can be of order 10^4.

2. Experimental configuration

The visible-light diagnostic beam line at SPEAR3 was designed to study the properties of the electron and SR photon beams. As the unfocused SR light propagates from the source it first encounters a four sided 'picture-frame' rectangular aperture located $\sim$7 m from the source which limit the angular acceptance of the beam line to 3.5 mrad (H) × 6 mrad (V). A water-cooled copper 'cold finger' further blocks the high power X-ray and partially visible components of the SR in the horizontal mid-plane by $\pm$0.47 mrad. The visible component passing through these apertures is reflected by a Rh-coated extraction mirror at 81° incidence angle from the surface normal. The angular acceptance of this mirror is larger than that of the upstream apertures. The first focusing lens of the measurement system is a 6" diameter BK7 doublet lens with a focal length of f=2 m to generate a virtual image plane of the SR source on the optical bench.

Following the basic optical setup of previous experiments [3,4,14], the DMD imaging system at SPEAR3 is composed of two functionally separate optical channels. Channel 1 images the

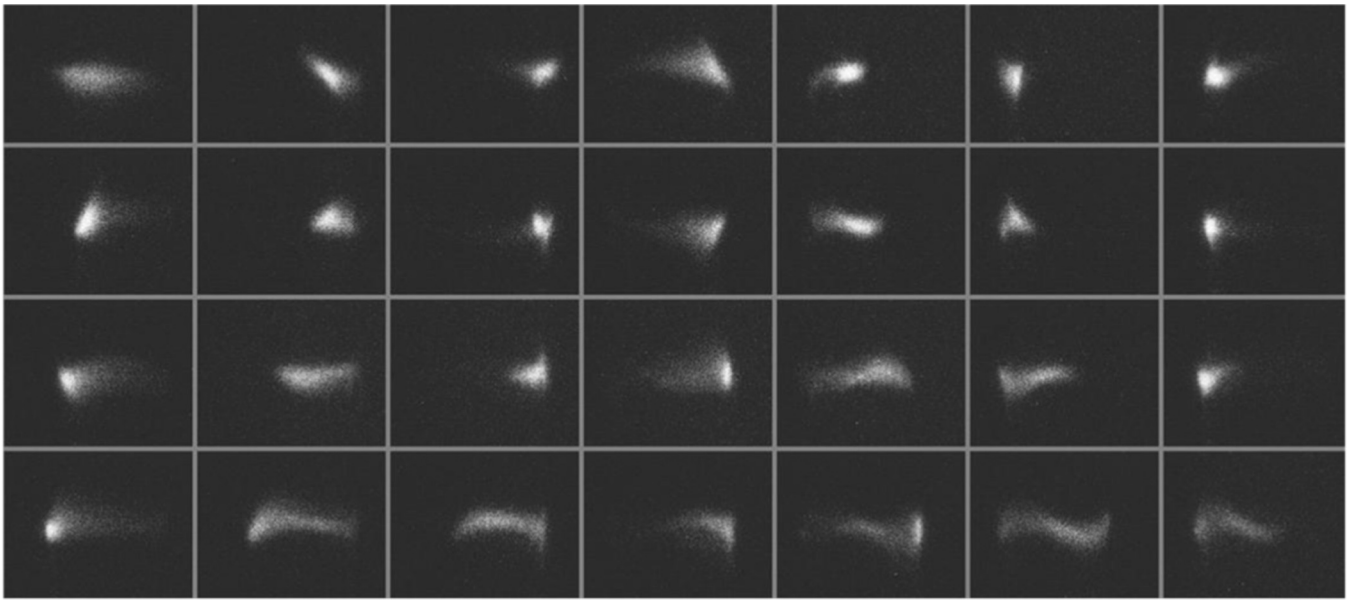

Fig. 1. Turn-by-turn images of charge injected into SPEAR3 with no stored beam present. Turn count progresses from left to right along rows beginning in the upper left corner. Maximum left-to-right pulse excursion is approximately $\pm$8 mm [12].

source onto the DMD surface and Channel 2 images the DMD surface onto an image-intensified CCD camera (ICCD). A schematic of the optical system is shown in Fig. 2. In terms of magnification at the DMD the visible SR is first focused by the $f=2$ m objective lens (150 mm-diameter) to form an intermediate image with a demagnification $M1=0.138$. The beam is then reimaged with a magnification of $M2=3.55$ onto the DMD at the end of Channel 1. The net magnification between the visible SR source point and the DMD surface is therefore $M1^{*}M2=0.493$. This value was chosen to provide a sufficiently wide field of view to observe the ± 8 mm horizontal oscillations of the injected beam in the source plane (see Fig. 1).

Channel 2 consists of a single 2-in. diameter, 1:1 achromatic lens with focal length $f=100$ mm. The high numerical aperture collects the zero- and first diffraction orders radiated by the 2D 'grating' structure of the DMD mirror array [15]. Previous studies have demonstrated that up to 90% of the light reflected by the DMD is contained in these first two orders and that rejection of higher orders has a negligible effect on image quality. A focusing lens relays the DMD image with unity magnification ($M3=1.0$) onto the ICCD camera input window with minimal chromatic aberration.

Due to the mechanical construction of the DMD array and the associated beam line optics, two geometric compensations must be applied. The first is a simple 45° rotation of the DMD mirror about the optical axis to align the 'flipping' axes of the micro-mirrors, which lie along the diagonal of each mirror, with the vertical direction. The second compensation requires a rotation of the ICCD camera about the vertical axis by the so called *Scheimpflug* angle [16] in order to compensate for the projected source plane of the DMD as seen by the camera focused onto the plane of the DMD when its micro-mirrors are rotated +12° (see Fig. 3). This *Scheimpflug* angle is given by $\varphi = \arctan(\frac{v}{u}\tan\theta)$, where θ is angle between DMD surface and axis of the 1:1 lens, and u and v are the DMD-to-lens and lens-to-camera distances measured along the optical axis, respectively. Here, v/u is equal to the inverse of the magnification which is unity and $\theta=24°$, so that $\varphi=24°$. Fig. 3 schematically illustrates the micro-mirror positions when they are reflecting into the second channel.

The ICCD (PiMax camera) used for these experiments features a fast-gated photocathode, an 18 mm diameter micro-channel plate image intensifier (MCP) and a tapered fiber optic bundle which couples a phosphor screen output window to a 1024×1024 pixel CCD array. The fast electronic gating feature of the photocathode was used to isolate injected charge pulses in time on a turn-by-turn basis.

The masks on the DMD to block the stored beam were constructed by first inserting a strong neutral density filter into the beam with all the DMD micro-mirrors set to reflect the full beam image, including the bright stored beam onto the CCD. Two types of optical masks were generated to spatially filter the image. The first was a simple geometric shape, e.g. a rectangle, polygon or circle with user-specified dimensions. The second was based on an intensity threshold algorithm applied to the measured image. For this case, we wrote a MATLAB program that located all points in the image with intensity value higher than the user-specified

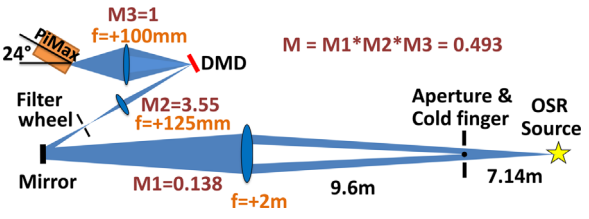

Fig. 2. Schematic optical arrangement for DMD mask experiments.

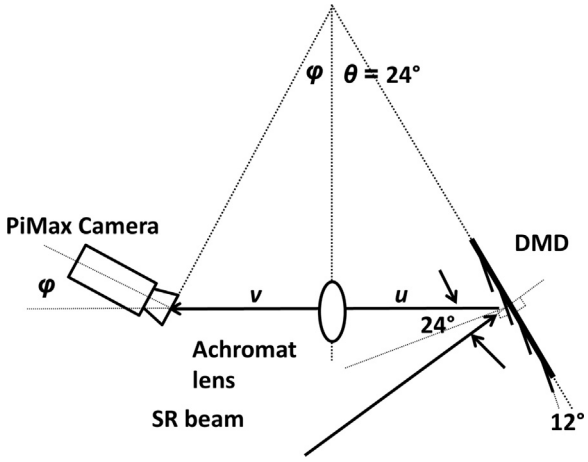

Fig. 3. Geometric construction of *Scheimpflug* angle for the micro-mirror array.

threshold value and then transformed these points to the corresponding points (pixels) on the DMD. A binary mask was then generated on the DMD, i.e. each pixel was flipped either +12° or -12° to direct the incoming light either onto the PIMAX camera or 48° away and thus out of the second optical channel.

Once the initial mask was applied, the neutral density filter strength was progressively reduced, the integrated number of camera acquisition frames was increased and increasingly more aggressive beam intensity masks created. A fixed, high-gain setting was used for the MCP during this procedure. In practice, the transverse mask coordinates were fine-tuned in software to precisely align the mask with the SR beam pattern. Finally the number of integrated camera exposures was set to obtain an image of the beam halo or injected beam, close to, but not exceeding the pixel saturation level. In principle this process can be repeated until the beam halo image measurements cover the entire surface area of the DMD.

To create a composite high dynamic range image of the beam, a series of masked images were obtained by progressively lowering the intensity threshold for creating the mask. Each masked image views only the beam profile below the set threshold using the full dynamic range of the ICCD sensor by integrating a proper number of camera frames. Then by normalizing each image to the number of acquisition frames, a composite image was generated with an effective dynamic range that exceeds the dynamic range of any individual image. In this manner many types of high-grade cameras can in principle be used to effectively stretch the dynamic range by orders of magnitude beyond the inherent limit of the optical system, which is usually limited by stray light, intrinsic dynamic range, camera read out noise and other effects to $<10^3$ [1]. Using the DMD based masking technique, we have previously demonstrated effective dynamic ranges exceeding 10^5 and in the present study we achieved an effective dynamic range greater than 10^6.

3. Point spread function

For our system, the PSF of the optical transport system is chiefly determined by the limiting apertures upstream of the first objective rather than any visible optical element in the system. For example the light beam accepted by the first lens in the system falls well within the area of the first lens and is not diffracted by the periphery of the objective. Therefor the PSF of the system is dominated by the upstream apertures. In order to compare the features of the experimentally measured PSF with simulations, we developed a computer code to calculate the 2-D visible SR

intensity distribution imaged onto the camera, starting with the Fraunhofer or far-field approximation of the SR source observed at the first objective lens ($f=2$ m) of the optical line. We then imposed a generalized pupil function in the principal plane of the lens with the same shape and angular acceptance as the visible light field distribution seen at the input to the lens.

The code calculates the PSF produced by the lens assuming that the pupil function is illuminated by visible SR produced by a single electron at the source plane using the standard wave optics approach [17]. Note that this visible SR is not the same as that produced by an ideal point source, usually featured in optics texts, which has a uniform angular distribution. Here the 'point' source of the SR is that produced by a single electron as it moves along an arc. Thus the 'point' source is rather a line source that is designated by the arc length observed by the first limiting aperture of the optical system. However, if the solid angle of the observed radiation is small and the region of the arc from which the radiation emanates is short, then observed radiation is a good approximation to an optical point source. For these calculations the length of the observed electron beam trajectory is about 30 mm, the sagitta of the trajectory is 140 μm, and solid angle of observation is 3.5 mrad (H) × 6.0 mrad (V) as defined by the first limiting aperture in the beam line. Hence, the point source approximation is quite good for our application.

3.1. PSF results

The unfocused SR beam seen in the left side of Fig. 4 shows a broad band intensity distribution (i.e. the generalized pupil function) observed at the input plane of the 2 m focusing length objective lens in the beam line. The light distribution clearly shows the 3.5 mrad (H) × 6.0 mrad (V) angular field of view defined by upstream beam line apertures. We interpret this distribution as the Fresnel or near field diffraction pattern resulting from the limiting beam line apertures that are illuminated by the point like visible SR. Note that the ~60 mm (H) × 100 mm (V) intensity distribution is contained well within the circumference of the 150 mm objective lens. Hence, there is little if any diffraction from the circular pupil function of the lens.

By imaging the unfocused white light onto the DMD and creating a series of intensity threshold masks as described above, it was possible to obtain the composite, high dynamic-range (~10^6) image of the stored beam, which is shown in the pseudo-color image to the right side of Fig. 4. The cross-like structure, seen in the image, is the diffraction pattern theoretically expected from a rectangular aperture [17]. Note, however, an additional 'slanted' ray diffraction pattern displays in the upper right quadrant of this image. This feature is due to diffraction from the inclined edge of a misaligned absorber seen in the upper right corner of Fig. 4 (left).

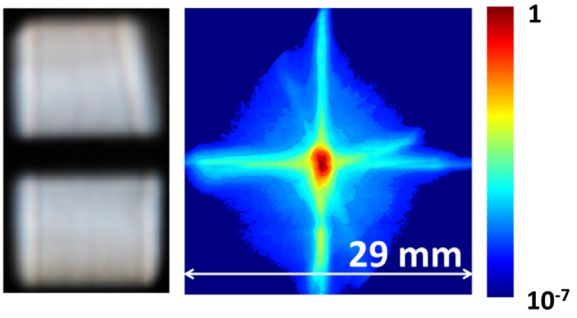

Fig. 4. (left) broad-band intensity distribution of white light measured at the first objective lens; image size is 59 mm × 102 mm with a 20 mm wide central shadow; (right) re-imaged log-normal intensity profile of the stored beam showing first 7 decades. Size of the image referred to the source plane is 29 mm × 29 mm; psuedo color bar scale shows logarithmically increasing intensity from blue to red. (For interpretation of the references to color in this figure legend, the reader is referred to the web version of this article)

Fig. 5 (left) shows the calculated generalized pupil function (GPF) based on a rectangular mask with the same angular acceptance as the real beam line aperture and illuminated by the visible SR produced by a single electron at one wavelength $\lambda=600$ nm. The total GPF is mathematically composed of the integral sum of GPFs over the camera sensitivity wavelength ban of 300–800 nm. The ratio of the horizontal polarized component (SR σ mode) to vertically polarized component (SR π mode) was taken to be unity based on direct measurements reported in [18]. For this application we ignored the wavelength dependence for the camera quantum efficiency and in the beam transport system.

A highly magnified view of the PSF calculated from the sum of GPFs over wavelengths weighted by the wavelength-dependent reflectivity of the Rh extraction mirror is shown on the right side of Fig. 5. This calculated PSF recreates all of the main features of the measured PSF shown in Fig. 4 (right), including the cross shaped aperture diffraction and inclined ray. The bluring in the measured PSF can be attributed to chromatic and spherical aberrations in the optical system, especially from characteristics of the BK7 objective lens not included in the simulation.

A comparison between the calculated PSF from the rectangular beam apertures in the wavelength band 300–900 nm and a real image of the stored beam is shown in Fig. 6 for the first 3 decades of intensity. Gaussian fitting of the measured horizontal and vertical line scans shows the RMS PSF sizes are approximately 400 μm and 800 μm.

A zoomed image of the calculated PSF is shown in Fig. 7. If we again fit a Gaussian profile to line scans taken through the center of this distribution the horizontal and vertical rms beam sizes are $\sigma_x=40$ μm and $\sigma_y=20$ μm, respectively.

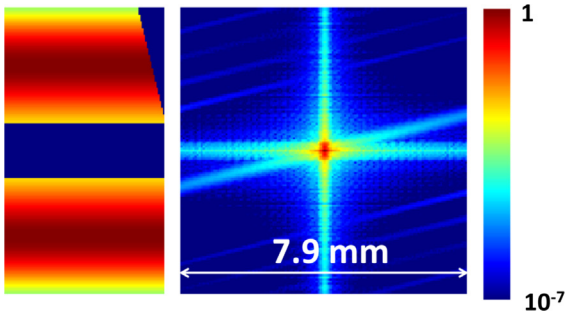

Fig. 5. (Left) simulated aperture function illuminated with theoretically calculated horizontal and vertical polarization components of visible SR at 600 nm. The image intensity is scaled according to the color bar increasing from blue to red; (Right) calculated wide band (300–900 nm) PSF with 7 orders of intensity scaled logarithmically according to the color bar. (For interpretation of the references to color in this figure legend, the reader is referred to the web version of this article.).

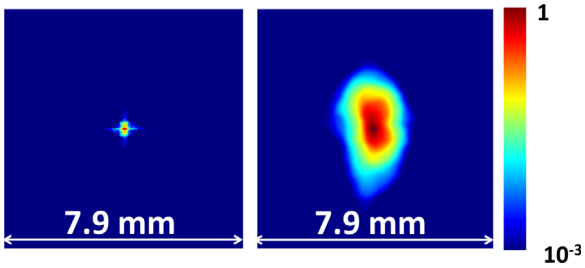

Fig. 6. (left) Close up image of the calculated PSF; (right) close up image of the stored beam at SPEAR3. Both show the first three decades of intensity (logarithmically scaled).

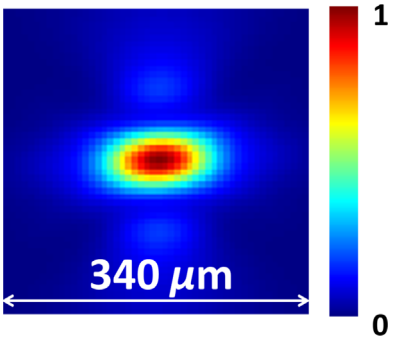

Fig. 7. Zoomed image of the calculated PSF with a linear scale of intensity.

The discrepancy between measurement and calculation is again attributed to wave-front distortion in the optical beam line as well as the errors introduced by visible bandwith of the synchrotron radiation, depth of field, curvature and diffraction. The design source size as confirmed by X-ray pinhole camera measurements and double-slit interferometry in the visible regime is $\sim$140 μm (H) × 20 μm (V).

In previous beam halo studies at UMER [3] and JLAB [4], the measured and calculated PSF values were used as a reference for the measurements of the beam halo. In both these cases the part of the image intensity lying above the PSF was considered the true beam halo. Otherwise, it was regarded as an artifact. In the present study, we can use the measured PSF image as in Fig. 4 to assist in determining what portion of the injected beam image is valid. If the injected beam signal is outside the stored beam mask and has an intensity level above the wings of the stored beam PSF we regard the stored beam PSF as background and subtract it to obtain the injected beam image. This is often the case for early turns after initial injection.

4. Measurements of the injected beam

One of the main goals of the SPEAR3 beam masking experiments was to image the transverse injected charge distribution in the presence of stored beam. The injected beam is produced by a 10 Hz booster synchrotron with up to 80 pC per pulse targeting one SPEAR3 bucket at a time. A schematic diagram of the accelerator system is shown in Fig. 8.

At each injection cycle, a single 3 GeV electron bunch enters SPEAR3 through a vertically-deflecting 'Lambertson septum' magnet within a pulsed horizontal beam bump. The injected beam is initially displaced -12 mm from the stored beam at the septum location and undergoes ± 8 mm horizontal betatron oscillations when viewed at the source point of the visible diagnostic beam line.

At only 80 pC per pulse, the injected beam does not radiate enough SR power to generate a clear image on the ICCD on a single pass. However, by synchronously gating the ICCD photocathode, it was possible to integrate multiple exposures of the injected charge for a given turn in a single camera frame prior to image readout. As indicated in Fig. 9, by physically masking SR radiation from the stored beam with the DMD and simultaneously time-gating the ICCD camera, most of the bright SR light radiated from the stored beam core can be rejected. Typically 15 superimposed exposures are sufficient to obtain an observable image of the injected beam. An additional mechanical shutter was used to further block visible SR during the 100 ms time interval between injection pulses and camera readout.

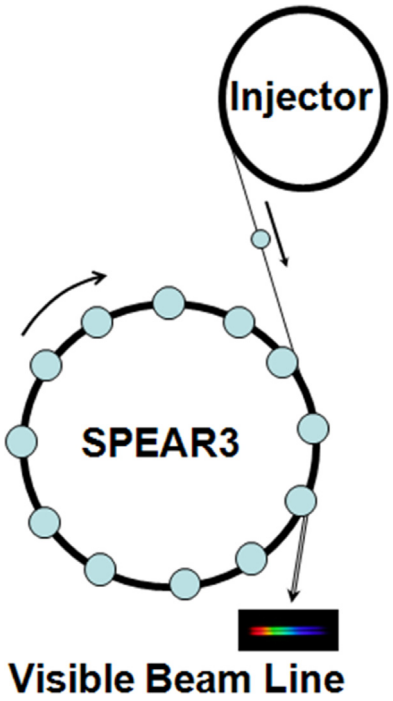

Fig. 8. Schematic of the injector, main ring and visible diagnostic line.

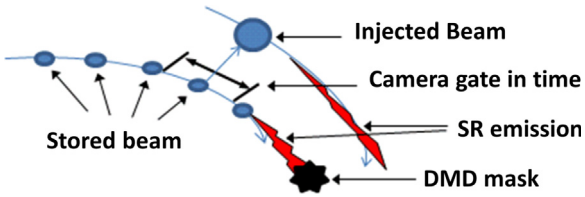

Fig. 9. Spatial masking and temporal gating of stored beam SR.

4.1. Baseline measurements

For the first set of baseline measurements, $\sim$50 pC electron pulses were injected into 15 symmetric buckets around the storage ring during the charge accumulation process. This 'clock mode' injection scenario allows us to: 1) keep the stored beam current in each bunch nearly constant and 2) ensure the final stored charge in any one bunch does not dominant the charge in other bunches. Clock mode injection also minimizes any effect of the stored beam influencing injected beam dynamics. Clock mode progressive injection is also the default for top-up during User operations. In 'clock mode' accumulation, the PiMax camera timing gate was set to open for 10 ns in synchronism with the each injected beam pulse. The camera gate automatically advances from target-bunch to target-bunch at the 10 Hz injection frequency as it tracks the master timing trigger (see Appendix A for a description of the camera timing system).

An example of clock-mode imaging of the injected beam is illustrated in Fig. 10. The data shows the first 6 turns of the injected beam using a rectangular mask which can be seen to eclipse the injected beam image depending on the betatron oscillation phase.

In the alternative 'stack mode' method, injection is programmed to target multiple shots into a single SPEAR3 bucket before advancing. The camera timing for 'stack mode' injection is less complex but high stored charge in a single bucket results in a high background SR signal. This can flood the DMD intensity mask, saturate the camera and potentially influence injected beam dynamics.

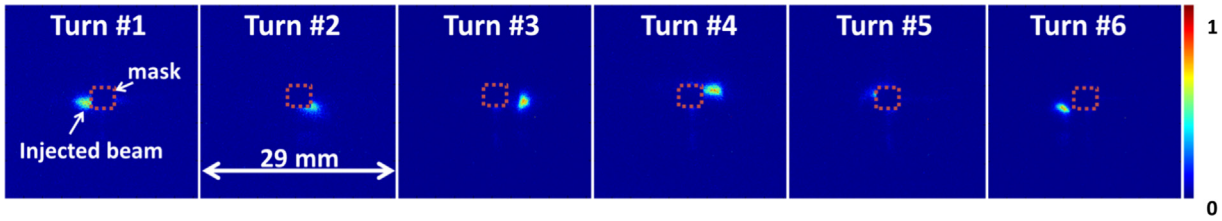

Fig. 10. First 6 turns of the injected beam imaged with rectangular mask (nomalized linear scale).

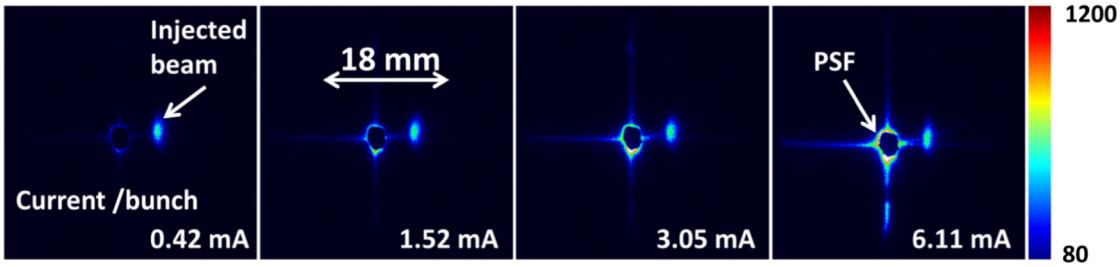

Fig. 11. Injected beam images (in linear scale) for the sixth turn after injection with increasing stored beam current initially in the bunch (linear scale).

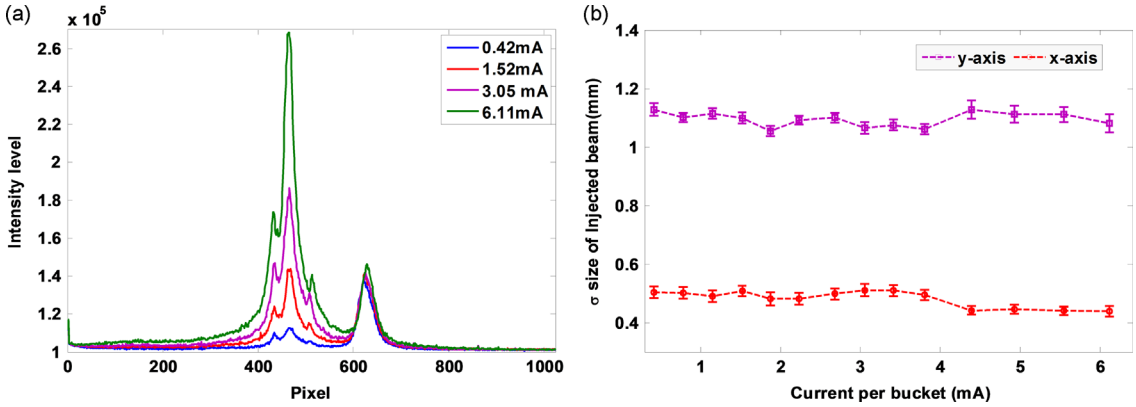

Fig. 12. (a) Typical beam profile lineouts demonstrating growth of the PSF intensity as the stored beam current increases with constant intensity of the injected beam; (b) injected beam size as a function of stored beam current.

An example using a dynamic-intensity DMD mask in stack mode injection is shown in Fig. 11. In this case, the four images show the injected charge on the same turn with increasing values of stored beam current in the target bunch. Each image is again a superposition of 15 exposures. Note that the 'cross' shape of PSF becomes increasingly pronounced as the stored beam in the bunch increases and the bright SR signal begins to flood the mask. Clearly, with increasing beam current, light from the PSF becomes more prominent while the ~50 pC injected beam intensity remains constant.

The horizontal projection for these four images is shown in Fig. 12 (a), with the rms beam size of the injected charge shown in Fig. 12 (b). The beam sizes are obtained from Gaussian fit. We calculate the error for beam size based Gaussian fitting error as well as systematic error [10] which including chromatic error, depth of field error, curvature error and diffraction error. The fitting error varies case by case, and the systematic error is estimated as 60 μm for each case in a r.m.s. sense. The successful imaging of injected beam with a 6.11 mA stored beam in a single bunch provided the first evidence that injected beam imaging was possible in a normal User operation mode with 500 mA stored beam current. Significantly the injected beam capture dynamics does not appear to be affected by the stored beam. In 500 mA User mode with ~1.4 mA per bunch, fast camera gating over 3–4 bunches (~10 ns) is equivalent to gating on an isolated 6 mA bunch in the sense of the PSF intensity from the stored beam.

4.2. Production measurements

During User operations, the injection top-up cycle occurs every 5 minutes with 30–40 pulses required to replace ~5 mA stored beam loss. Using the 15-pulse multiple-image exposure technique, it was therefore possible to acquire images of injected charge on 2 separate turns each top-up cycle.

By applying the intensity threshold masking technique, we acquired injected beam images for the first forty turns over a series of top-up injection cycles. Examples of measurements taken for discrete turns are shown in Fig. 13. In this case the intensity mask threshold level was set to block out the stored beam signal including positional jitter induced by any mismatch of the pulsed injection system kicker magnets. Since the DMD mask position is fixed, for some turns portions of the bright stored beam SR component become more visible along with a shift of the associated PSF. For turns 22 and 26 it was necessary to compensate stored beam orbit jitter by using a larger mask.

For each turn, the acquired image shows the mask covers the intense core of the SR beam, the injected beam and portions of the stored beam PSF outside the DMD intensity mask. In the data analysis, we treat the PSF outside the mask as background. By

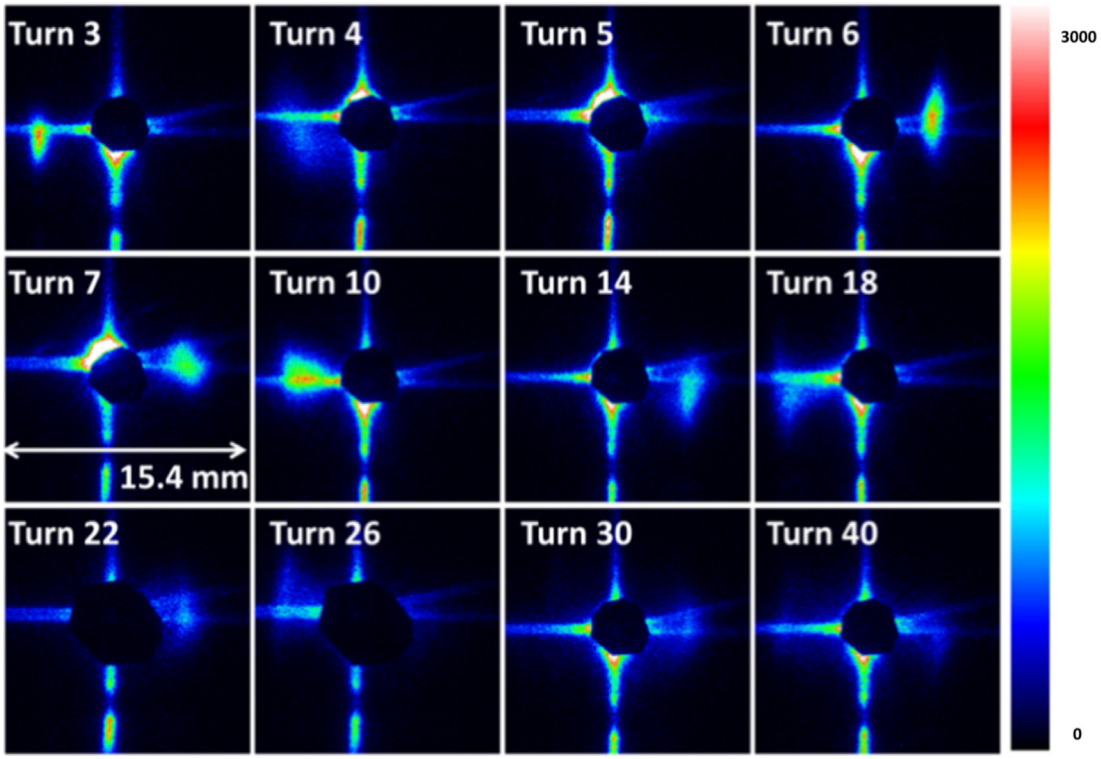

Fig. 13. Raw images of injected beam at the visible SR view port for different turns with intensity mask applied to the stored beam image during normal operation (linear scale).

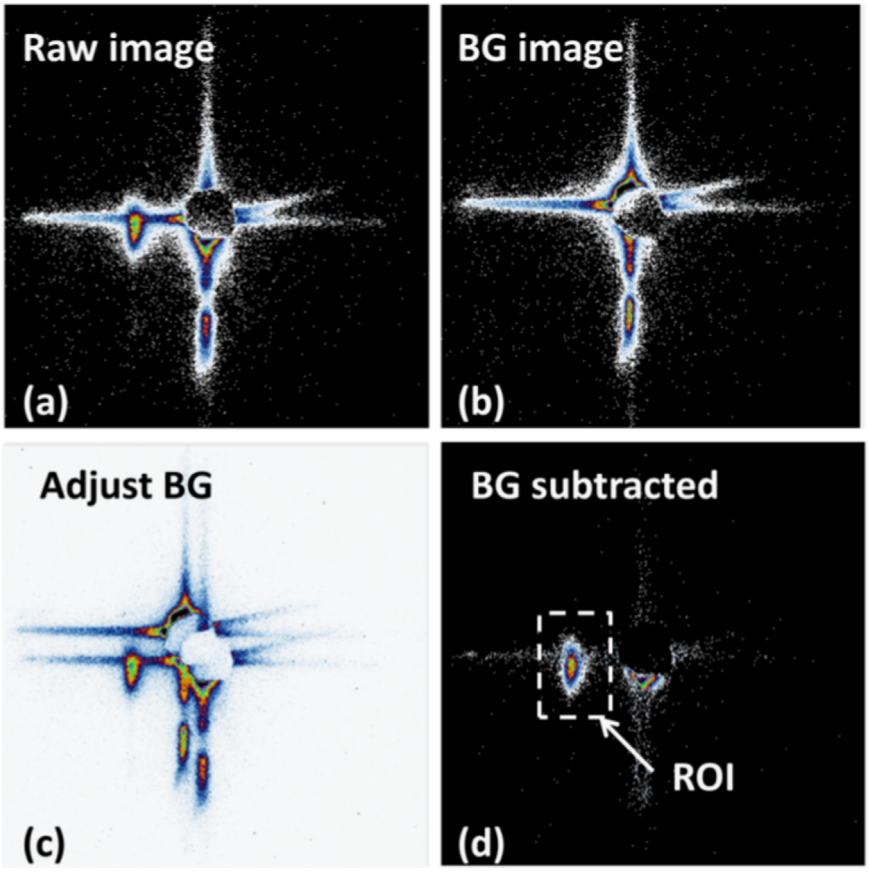

Fig. 14. Illustration of the background subtraction process.

performing background subtraction, most of the PSF can be eliminated and the contrast improved for the injected beam.

Detail of the background subtraction process is illustrated in Fig. 14. In this case some stored beam positional jitter is apparent as can be seen by comparing movement of the associated PSF seen in Fig. 14 (a) and (b) noting that the mask location is fixed. The data indicates that at times background subtraction is not straightforward with a single universal background image, even with the same camera and intensity mask settings. If the injection kickers are not precisely balanced, for example, the stored beam will exhibit residual betatron motion from turn-to-turn. Although this effect can be blocked by applying a larger mask, movement of the associated PSF pattern makes background subtraction less effective. Thus, to effectively use background subtraction to image the injected beam charge distribution, it may be necessary to acquire a background image specific to each turn. In practice this process can be time consuming. To simplify the process, noting that the PSF outside the intensity mask has a nearly constant profile, we can alternatively use a single background image (see Fig. 14 (b)) and adjust both intensity and position in software to cancel the diffraction pattern in the raw image. An example using the software-adjusted background subtraction technique is shown in Fig. 14 (d).

By using the results from 'background' subtraction imaging, the injected beam centroid and RMS beam size extracted from the measured distributions are plotted in Fig. 15. As the injected beam circulates around the storage ring, the charge distribution progressively decoheres in phase space so that the Gaussian fit to beam size becomes less meaningful.

4.3. Beta function matching

For optimum injection efficiency, the beta-functions and the sigma matrix in the BTS should be matched to the storage ring [19]. One effective approach to study matching conditions is to systematically adjust the transport line optics while monitoring the turn-by-turn profile of the injected beam. To test this procedure we tuned a defocusing quadrupole QD9 near the end of the BTS and measured the impact on the turn-by-turn injected beam profile. Clock-mode image acquisition was used with a rectangular DMD mask. Fig. 16 shows the injected beam every second pass for the first 20 turns for three different QD9 quadrupole settings. The resulting storage ring injection rate is indicated to the right of the plot for each measurement.

The data clearly shows that as the mismatch increases the injection rated decreases and the injected beam diffuses after only a small number of turns. For turns that have relatively well-defined images (6, 10 and 18) there is a linear relation between image intensity and the injection efficiency indicating some beam loss occurs between QD9 and the injection septum as well as on early turns in the accumulation process. At the time of these measurements the injection kickers were slightly mistuned causing the stored beam to exhibit low-amplitude horizontal betatron oscillations. As a result the PSF pattern also moved and a DMD mask with large coverage in the horizontal plane was necessary.

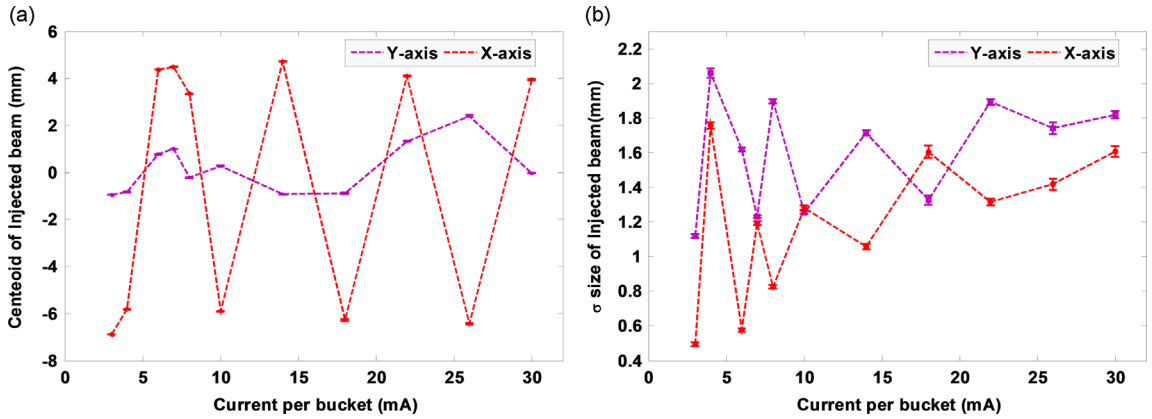

Fig. 15. Turn by turn evolution of beam centroid (a) and transverse beam size and (b) during normal operations. Nominal beam damping times ~4000 turns.

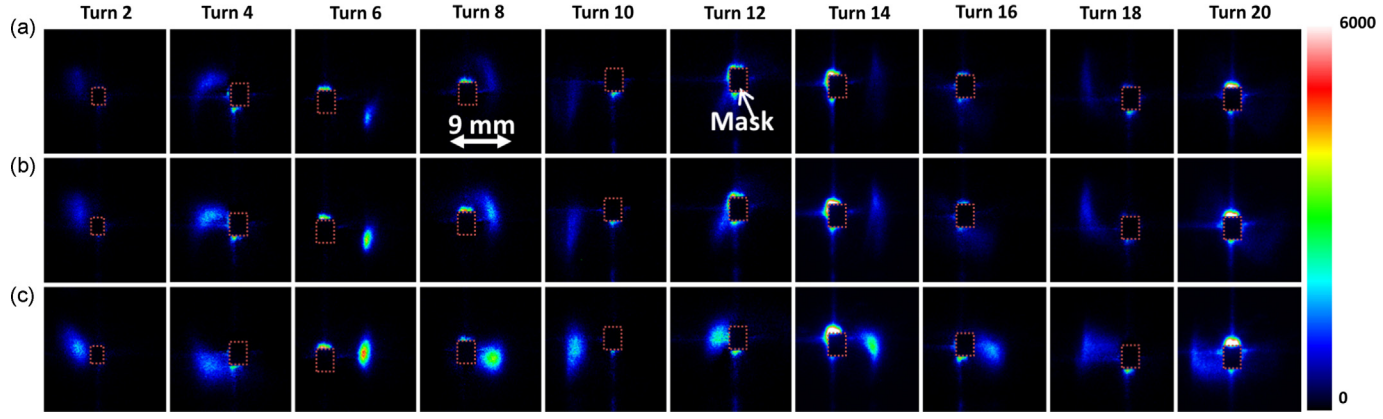

Fig. 16. Turn-by-turn profile of injected beam for three different defocusing quadrupole settings in the BTS transport line (QD9): (a) QD9 current 14.90 A, injection rate 15.3 mA/min; (b) QD9 current 17.46 mA, injection rate 33.0 mA/min; (c) QD9 current at the default setting, final injection rate 61.0 mA/min.

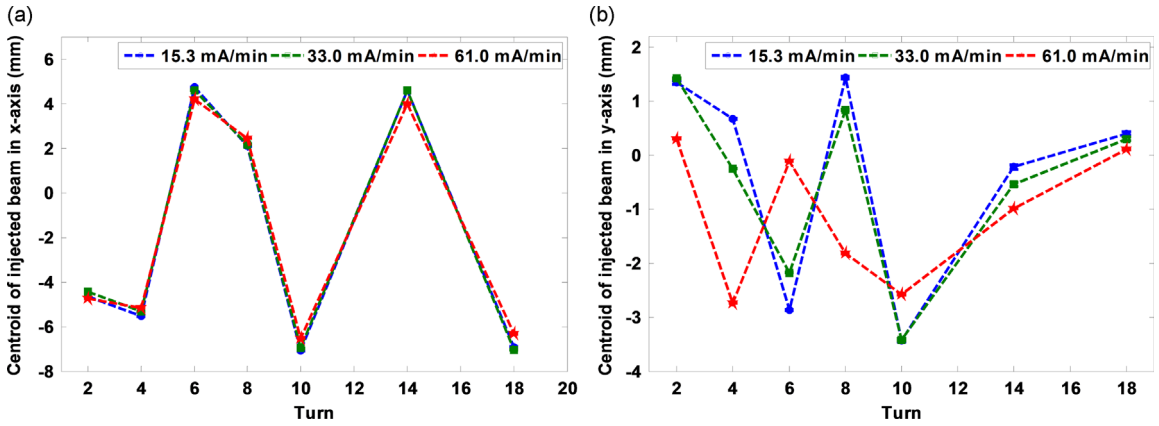

Fig. 17. Injected beam centroid motion for the three settings of a de-focusing BTS quadrupole: (a) *x*-axis; (b)*y*-axis.

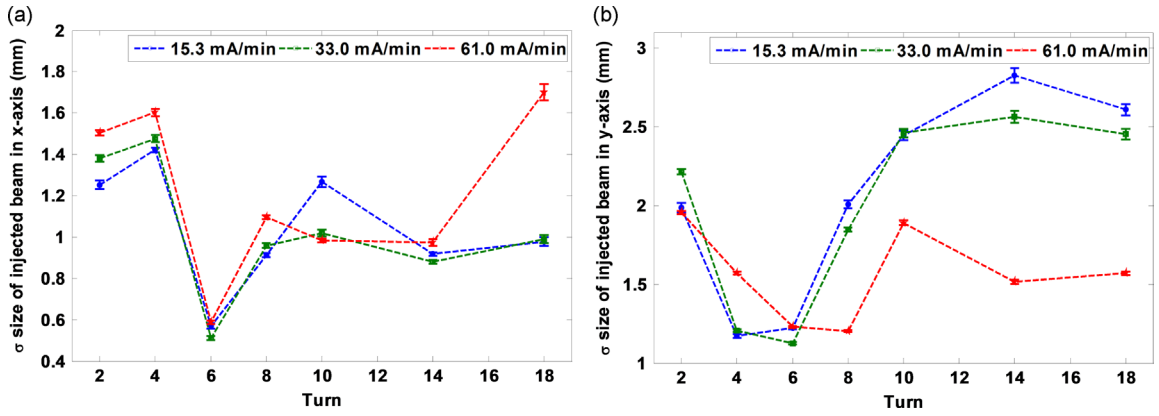

Fig. 18. Turn-by-turn injected beam size for three settings of de-focusing BTS quadrupole QD9: (a) *x*-axis; (b)*y*-axis.

Fig. 17 shows the calculated beam centroid position as a function of turn number. By design, the horizontal oscillation amplitude is large while the non-zero vertical oscillation amplitude indicates an injection angle error which increases as we decreased the field in QD9. This behavior is indicative of a vertical beam offset error in the magnet.

Fig. 18 shows the beam size of the charge distribution at each turn. Initially the relatively round beam has a similar size in both planes but the time evolution in phase space is different along the *x* and *y* coordinates during the charge capture process. The beam size values are suppressed for turns 12, 16 and 20 due interference from the DMD mask.

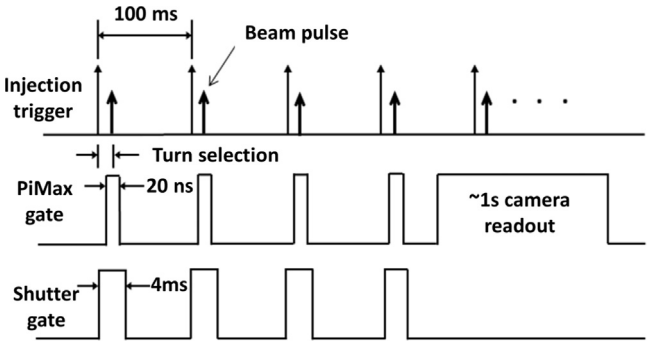

Fig. 19. Schematic timing diagram for four-pulse exposure of injected beam image.

5. Conclusions

This paper demonstrates application of a digital micro-mirror array device to optically mask the visible component of synchrotron radiation from an electron beam storage ring, SPEAR3. The DMD mask blocks the bright visible SR emission of the stored beam core, so that one can measure the characteristic PSF of the optical beam line and the time evolution of injected beam in presence of the stored beam. The point spread function of the optical beam line was measured with dynamic range of order 10^6 using the stored beam as an effective point source. When the fast-gating feature of the image-intensified camera was applied in conjunction with the physical DMD mask, it was possible to image the injected beam in the presence of a high intensity stored beam. The measurements were conducted during both dedicated machine development time and User operations. Examination of the transverse injected beam profile can provide experimental insight into the processes of non-linear phase-space decoherence of the circulating charge distribution. In the future we plan to refine the data acquisition process to improve reconstruction of the injected beam profile in regions where the light is either blocked by the DMD mask or completely obscured by the PSF. This work will likely require a modified Lyot stop and/or spatial filtering to mitigate diffraction effects from the upstream beam line apertures. The DMD masking method for injected beam viewing is useful for matching the BTS to the storage ring which can lead to improved beam capture efficiency. This may also find application as SPEAR3 moves toward a low emittance lattice with reduced dynamic aperture and pseudo bunch [20].

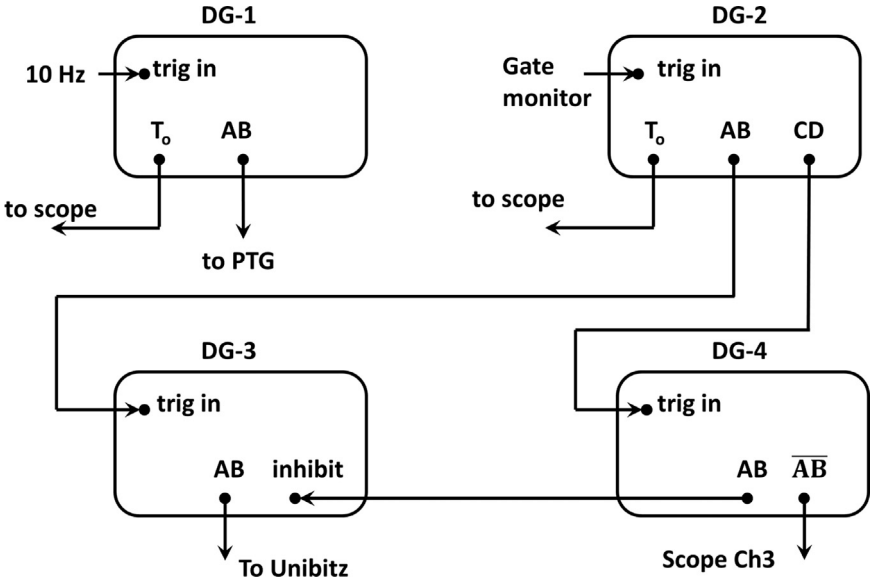

Fig. 20. Trigger delay system for PiMax Pulse Trigger Generator and mechanical shutter.

Acknowledgments

The authors would like to thank T. Mitsuhashi for technical discussions regarding coronagraph measurements and the optical system. The SPEAR3 operations team provided excellent on-demand beam quality under challenging measurement conditions.

Appendix A. Camera timing system

To isolate a single turn of injected charge in the storage ring, the PIMAX camera must be gated synchronously with the passage of the bunch. As indicated in rows 1 and 2 of the timing diagram shown in Fig. 18, the 10 Hz injection kicker trigger is used as a pre-trigger to the electronic camera shutter. The fast-gated the camera shutter only opens long enough to collect light as the injected charge passes including light from a few neighboring bunches. Unwanted light emitted by the rest of the bunch train and subsequent bunch train revolutions around the storage ring is gated and does not contribute to the image. Signal integration is accomplished by acquiring multiple exposures in software prior to readout of a single image frame. Selection of the injected charge turn number is made either by manual adjustment at the delay generator or by using the PIMAX data acquisition 'sequencing' feature under software control.

In practice the extinction ratio resulting from the gating action of the PIMAX photocathode is approximately 10^6 due to light leakage through the photocathode assembly. During the 100 ms time interval between 10 Hz camera gates, visible SR light from $\sim 3x10^7$ bunch pulses enters the diagnostic beam line and impinges on the camera photocathode. Since the camera contrast ratio is not sufficient to completely reject the background light a mechanical shutter was added in the beam line. As indicated in row 3 of Fig. 19, the mechanical shutter provides an additional 4 ms time gate capability to improve the contrast ratio. The mechanical shutter also blocks light during the $\sim$1s camera readout interval.

The overall timing sequence was implemented using four SRS DG535 delay generators (DG). As illustrated schematically in Fig. 20, DG-1 receives the 10 Hz injection kicker trigger from SPEAR3 and provides a fixed-delay trigger to the PIMAX's Pulse Timing Generator (PTG). For the first pass of the injected beam the PTG camera gate is delayed 321 ns. For subsequent turns, the delay time is set to $321+(n-1)*781$ ns, where '*n*' is the turn number and 781 ns is the bunch revolution period. The PTG operates under software control to set the image exposure duration, number of exposures per image and can 'sequence' image acquisition with progressive time delays. When the 'Acquire' command is issued in software the camera responds to input triggers until the image acquisition cycle is complete.

Fig. 20 also shows how the mechanical shutter is controlled by the combined action of 3 auxiliary delay generators. In this case DG-2 is triggered by a TTL output pulse from the PIMAX camera at each photocathode gating cycle. DG-2 provides the appropriate delay to the next 10 Hz beam pulse and commands DG-3 to open a Uniblitz mechanical shutter for 4 ms. DG-2 also triggers DG-4 which inhibits the mechanical shutter during the image readout cycle. In this configuration the first injected beam pulse is not acquired but background visible SR emission between injection pulses and during the frame readout period is eliminated.

References

[1] T. Mitsuhashi. Proceedings of DIPAC, Lyon, France, 2005, pp. 7.
[2] T. Mitsuhashi. Proceedings of EPAC, Lucerne Switzerland, 2004, pp. 2655.
[3] H.D. Zhang, R.B. Fiorito, A.G. Shkvarunets, R.A. Kishek, C.P. Welsch, Physical Review Accelerators and Beams 15 (2012) 072803.
[4] R. Fiorito, A. Shkvarunets, H. Zhang, D. Douglas, F. Wilson, S. Zhang, J. Corbett, A. Fisher, W. Mok, K. Tian, Proceedings of BIW 2012 Newport News, VA, USA, pp. 201.
[5] J. Corbett, T. Mitsuhashi (private communication).
[6] J. Corbett, W. Cheng, A.S. Fisher, E. Irish, T. Mitsuhashi, W. Mok, Proceedings of PAC, Vancouver, BC Canada, 2009, pp. 4018.
[7] A. Hofmann, F. Meot, Nuclear Instruments and Methods in Physics Research Section A 203 (1982) 483.
[8] A. Andersson, J. Tagger, Nuclear Instruments and Methods in Physics Research Section A 3 (64 , 1995) 4.
[9] U. Arp, Nuclear Instruments and Methods in Physics Research Section A 462 (2001) 568.
[10] J.C. Bergstrom, J.M. Vogt, Nuclear Instruments and Methods in Physics Research Section A 562 (2006) 495.
[11] A. Hansson, E. Wallen, A. Andersson, Nuclear Instruments and Methods in Physics Research Section A 671 (2012) 94.
[12] J. Corbett, W. Cheng, A.S. Fisher, X. Huang, W. Mok, J. Safranek, S. Westerman, Proceedings of BIW, Santa Fe, NM, USA, 2010, pp. 318.
[13] J. Corbett, W. Cheng, A. Fisher, W. Mok, S. Westerman, AIP Conference Proceedings, 1234, 251, 2010.

[14] H. Zhang, R. Fiorito, A. Shkvarunets, J. Corbett, K. Tian, A. Fisher, Proc. of IPAC, New Orleans, Louisana. USA, 2012, p. WEOAA01.
[15] DMD Discovery 4100 Controller Board and Starter Kit, Texas Instruments, Inc.
[16] T. Scheimpflug, GB Patent No. 1196 issued 12 May 1904, see also http://www.trenholm.org/hmmerk/#SR.
[17] Born, Wolf, Principles of Optics, 7th ed., Cambridge University Press, Cambridge, UK.
[18] C. Li, J. Corbett, T. Mistuhashi, Proceedings of IBIC, Melbourne, Australia, 2015.
[19] X. Huang, J. Safranek, W. Cheng, J. Corbett, J. Sebek, Proceedings of PAC, Vancouver BC, Canada, 2009, pp. 1641.
[20] G. Portmann, S. Kwiatkowski, D. Plate, J. Julian, R. Low, K. Baptiste, W. Barry, D. Robin, Proc. of PAC, Albuquerque, New Mexico, USA, 2007, p. TUPMN115.